remote sensing

MDPI

Article

Vegetation Mapping by Using GPM/DPR over the Mongolian Land

Baasankhuu Nyamsuren [1,2,*], Kenlo Nishida Nasahara [1,3], Takuji Kubota [4] and Takeshi Masaki [5]

1 Graduate School of Life and Environmental Sciences, University of Tsukuba, Tennoudai 1-1-1, Tsukuba 305-8572, Japan; nasahara.kenlo.gw@u.tsukuba.ac.jp
2 Information and Research Institute of Meteorology, Hydrology, and Environment (IRIMHE), Juulchiny street-5, Ulaanbaatar 15160, Mongolia
3 Faculty of Life and Environmental Sciences, University of Tsukuba, Tennoudai 1-1-1, Tsukuba 305-8572, Japan
4 Earth Observation Research Center, Japan Aerospace Exploration Agency (JAXA), Sengen 2-1-1, Tsukuba 305-8505, Japan; kubota.takuji@jaxa.jp
5 Remote Sensing Technology Center of Japan (RESTEC), Tennoudai 1-1-1, Tsukuba 305-8572, Japan; masaki_takeshi@restec.or.jp
* Correspondence: nyamkansn@gmail.com; Tel.: +81-29-853-4897

Received: 31 August 2019; Accepted: 9 October 2019; Published: 15 October 2019



Abstract: Mongolian steppe is one of the largest and important ecosystems. The degradation of grassland and the expansion of desert are occurring due to drought and desertification processes. We attempted monitoring of the broad-scale vegetation in Mongolia by a space-borne precipitation radar, which may complement typical approaches of vegetation monitoring (such as NDVI). We utilized the Global Precipitation Mission's (GPM) dual-frequency precipitation radar (DPR). We characterized backscatter (σ^0) of GPM/DPR's two microwave bands (Ku and Ka) with respect to the dominant vegetation zones (forest, grassland, desert). Both Ku and Ka radars' σ^0 values were investigated for incidence angle dependency and the seasonal variation. As a result, the use of multi-angle, multi-band observations of GPM/DPR could help to characterize the vegetation zones. Especially, the σ^0 at incidence angles between 1° and 8° represented useful characteristics of vegetation. Based on it, by using unsupervised clustering, we produced annual maps describing vegetation zones from 2014 to 2018. The result indicated that Mongolia experienced extensive changes in grassland and desert areas during the study years.

Keywords: vegetation mapping; Mongolia; GPM/DPR; backscatter; incidence angle

1. Introduction

Vegetation is an important component of the terrestrial ecosystem, water cycle, energy cycle, and the carbon cycle [1–4]. The Mongolian steppe is one of the largest and important grassland ecosystems, including roughly 2.6% of the total global grassland [5]. However, affected by climate change and anthropogenic activities, it is degrading over the recent decades, with its ecological sustainability facing a threat [2,5,6]. Satellite remote sensing is an effective tool for observation of the dynamics of vegetation, especially such a broad, arid region as Mongolian grassland.

In remote sensing, vegetation is commonly observed by optical radiometers, microwave radiometers, and synthetic aperture radars (SAR). Each of them has disadvantages which should be complemented by other approaches. Optical radiometers' data can derive vegetation indices such as normalized difference vegetation index (NDVI), which is defined and calculated by a function of spectral band reflectance, and indicates vegetation chlorophyll abundance [3,7,8]. NDVI has a

history of long-term observations with high temporal resolution. However, such optical indices are easily degraded by atmospheric particles, namely, clouds and aerosols, such as haze or smoke [9]. Those errors can be somehow mitigated by applying atmospheric correction using radiative transfer models (RTM), but it is not always sufficiently effective because RTM requires information about the atmospheric particles that is sometimes difficult to obtain. Moreover, the sensitivity of vegetation indices such as NDVI is limited in a small range of leaf area index (LAI) [4]. It is because the optical sensors only sense the top of the vegetation canopies. In such ways, the optical vegetation indices are sometimes not effective [10,11]. Moreover, NDVI is only sensitive to green parts of the vegetation and insensitive to woody parts or non-photosynthetic plants. NDVI is also influenced by diurnal and seasonal changes in solar directions.

Microwave radiometers provide vegetation optical depth (VOD, [12]), which indicates the vegetation water content in the total above-ground biomass by making use of attenuation of microwave radiation through vegetation canopy. The VOD is not influenced by clouds or aerosols. Like NDVI, there is a long record of VOD data with high temporal resolution. However, VOD's spatial resolution is much coarser (>10 km) than NDVI. In addition, VOD is insensitive to frozen vegetation below 0 °C temperature [4].

SAR is sensitive to the soil moisture [13,14], vegetation structures including wood, stem, and leaf, without any influences by clouds or aerosols. It provides images with a high spatial resolution (~10 m). The SAR observation also spans as long as two decades. However, its data archive has several gap periods and its temporal resolution is not high (e.g., several weeks to several months) [15]. Moreover, SAR's side-looking wide-angle causes serious geometric distortions, such as foreshortening, layover, and radar shadow.

To complement these disadvantages, we propose vegetation monitoring by a space-borne precipitation radar, namely, the dual-frequency precipitation radar (DPR) on the core satellite of Global Precipitation Mission (GPM), which consists of two radars: Ku-band radar (KuPR, 13.6 GHz) with a swath width of 245 km and Ka-band radar (KaPR, 35.55 GHz) with a swath width of 125 km [16,17]. KuPR succeeds the previous single Ku-band precipitation radar of Tropical Rainfall Measurement Mission (TRMM) [18,19].

The precipitation radars such as GPM/DPR and TRMM/PR have several advantages: It is not influenced by clouds and aerosols. It would have less saturation in vegetation canopies. It is not influenced by solar direction. It may detect both photosynthetic and non-photosynthetic plants. On the other hand, its disadvantages include low spatial resolution (~5 km), but it is still better than the VOD's spatial resolution (>10 km) [4,16]. The GPM core satellite flies in a non-sun-synchronous orbit at 65° inclination (note that in a 65° inclined orbit, the actual coverage of the DPR swath extends from 67°N to 67°S). The 65° orbit inclination was selected to offer a broad latitudinal coverage maintaining a sufficiently short precession period to sample diurnal variability within a season [16]. The temporal resolution of GPM/DPR is several days to 10 days, depending on the band and geographic area, but it can be worse if we use only certain incidence angles. It may be worse than VOD or NDVI.

Moreover, SAR is a radar and it has similar advantages to GPM/DPR mentioned above, and its spatial resolution is much higher than GPM/DPR. However, GPM/DPR's down-looking narrow-angle radar is mostly free from the problems of foreshortening, layover, and radar shadow. While SAR observes a target only at a single angle, GPM/DPR observes at multiple directions. While SAR's revisit time occurs mostly at the same local time, GPM/DPR has revisit at various local times, reducing sampling bias and providing diurnal information of vegetation statistically.

In the previous studies, the sensitivity of the Ku-band radar on TRMM/PR was inspected for vegetation in Africa [20] and over the global low-latitude lands [21]. Over the global low-latitude lands, normalized radar cross-section (NRCS), which is normally described as σ^0, decreased with increasing vegetation density, with high σ^0 at the north African desert [21]. Moreover, in Africa, a combination of σ^0 at incidence angles of 3-degree and 17-degree was proposed as a good indicator of vegetation classification [20].

In comparison to TRMM/PR, one of the advantages of the GPM/DPR is wider coverage due to its bigger inclination angle (65°) than TRMM (35°) [16,18,19]. Mongolia is inside the coverage of GPM/DPR, but not in the coverage of TRMM/PR. Additionally, GPM/DPR has Ka-band radar which was absent on TRMM/PR. Although the Mongolian land exhibits significant geographic gradient, an extreme climate with four seasons, and diverse vegetation zones [22,23], the 5-km coarse spatial resolution is not a serious problem for regular monitoring of such a vast land as Mongolia. These unique conditions of the study area provide a favorable opportunity of testing GPM/DPR as a vegetation sensor.

The objective of this study is to utilize the GPM/DPR for monitoring of Mongolian vegetation. The central concept is to analyze the sensitivity of backscatter (σ^0) of KuPR and KaPR to vegetation, particularly its dependency on the incidence angles. We checked it for different vegetation density types and seasons. Then we examined the possibility of distinguishing vegetation zones by using DPR, and finally, we produced annual vegetation maps of the years from 2014 to 2018.

2. Materials and Methods

2.1. Study Area and Vegetation Characteristics

The study area spans within the latitudes of 41°00′N–53°00′N and longitudes of 87°00′E–120°00′E (EPSG:4326-WGS84), covering the entire Mongolian territory. It includes parts of the Siberian taiga forest, the Central Asian steppe, and the Gobi Desert. The northern part is forest (~10%), the middle-eastern part is steppe grassland (~60%), and the south-western region is the Gobi Desert (~28%) [5,23–25].

The northern forest area has a subarctic climate with cool summer with an annual precipitation of 300–400 mm. It is dominated by broadleaf, needle-leaf forests and mixed meadow steppe with high canopy cover. In the central part of the northern forest, dark mountain taiga exists with coniferous trees (*Pinus sibirica, Picea obovata, Abies sibirica, Larix sibirica*). This dark mountain taiga is surrounded by lighter subtaiga with needle and deciduous broadleaf forests (*Larix sibirica, Pinus sylvestris, Betula platyphylla*) [26]. The middle part of Mongolian grassland steppe is predominantly herbaceous with vegetation cover of 10%~100%, mainly covered by species: *Stipa krylovii, Stipa grandis, Carex duriuscula*, and *Cleistogenes* spp. In grassland steppe, some mountainous areas are covered by forest-steppe consisting of *Larix sibirica* which are primarily limited to north-facing mountain slopes. The total annual precipitation of the grassland region is approximately 150–250 mm under the semi-arid climate. The desert area features a higher average temperature with low annual precipitation less than 50–100 mm, mostly covered by barren and sandy areas including the thin layer of xerophytic shrubs, perennial forbs, and xerophyte herbs [24,27–29]. The southern desert area includes saxaul forests, with 25% of the total forest area in Mongolia [30].

Vegetation growing season is the only summer (May to September) since roughly 85% of total annual precipitation occurs in this period [25,28]. The Mongolian vegetation, especially grassland, is vulnerable to harsh climate conditions and natural disasters such as severe drought, wildfire, and desertification [6,31]. Moreover, expansive grassland steppe is important for herding activity, hence overgrazing is a pressure for the vegetation [22]. Drought and desertification are causing degradation of the grassland and expansion of the desert [3]. The impact of climate change is predicted to increase, giving further stress and accelerating vegetation degradation over the next three decades [3,32]. Therefore, Mongolia has a strong demand for new and various approaches to vegetation monitoring.

2.2. GPM/DPR Data and Preprocessing

The GPM is a joint mission of NASA and JAXA, which provides next-generation observations of rainfall and snowfall worldwide [16,17]. The GPM core observatory was launched on 28 February, 2014. It flies along a non-sun-synchronous orbit at 65° inclination. The GPM/DPR consists of two types of precipitation radars, namely, KuPR and KaPR. They observe microwave backscatter from rain

and snow particles as well as from the land surface, which is used in a surface reference technique (SRT) [17]. Thus, it contains signals related to the land surface.

The KuPR is equipped with nadir-looking cross-track 49 scan beams with the incidence angles within +/−17°, which covers a 245-km scanning swath. The KaPR has two types of scans, namely, the matched scan (Ka_MS) and the high sensitivity scan (Ka_HS). The Ka_MS is spatially nested within the central part targets of the KuPR observations. It has 25 beams with incidence angles within +/−8.5°, providing a swath width of 125 km [17,33]. For all modes and both bands, the width of one beam scan is approximately 0.75°, which corresponds to a footprint of 5 km on the Earth surface [33]. In this study, the normalized radar cross-section (σ^0) of the KuPR (HDF5 dataset named as /NS/PRE/sigmaZeroMeasured) and KaPR (HDF5 dataset named as /MS/PRE/sigmaZeroMeasured) stored in the standard level 2 data files (version 06A, HDF5 format) were used between 2014 and 2018. These GPM/DPR data are free and available at https://gportal.jaxa.jp website.

We divided the area by pixels with a resolution of 0.05 degrees in both longitude and latitude directions. For a certain period of time (composite period), we collected the GPM/DPR σ^0 data at each pixel for each incidence-angle-bin (with intervals of 0.75°). The collected σ^0 values at each pixel and each angle-bin were averaged in a deci-bell (dB) unit. In this process, the σ^0 data acquired in rainy or snowy conditions were discarded because they may be influenced by the rain (or snow) particles and surface wetness. Because GPM is a precipitation radar, it can detect rain particles and snow particles (which are bigger than a certain size) without the influence of cloud particles. Therefore, each σ^0 value has a flag (the HDF5 dataset named as "/PRE/flagPrecip") of whether it was raining (snowing) or not. We used this flag data for discarding the rainy and snowy conditions.

As a result, we made a composite map which consists of σ^0 data observed at several different timings during a certain period of time. If this period is long, we can make a seamless map, but instead, we need to give up a fine temporal resolution. If a pixel does not have any chances of observation at an angle, the composite map on that pixel for that angle was assigned with "no data" value. Approximately 5% of all pixels were "no data" in the period of May−September for each year, each incidence angle, and each band. In this way, we can have a backscatter (σ^0) raster map at each single angle scan. We created such datasets for KuPR and KaPR separately. It means we have multi-band multi-angle σ^0 maps for our study. All the preprocessing was performed by an original C++ program and HDF5 library on Ubuntu Linux 16.04.

2.3. Ancillary Data and Reference Data

To inspect the GPM/DPR characteristics over the land surfaces, we need several ancillary pieces of data and reference data. The first one is a consistent vegetation cover map. We used the Climate Change Initiative (CCI) Global Land Cover Map 2015 (global static map) provided by the European Space Agency (ESA), with an equal-angle rectangular grid at 300-m spatial resolution product. Originally the ESA-CCI map has 22 landcover categories [34]. We regrouped them into major six categories: Water, urban, forest, grass, desert, and no data. The original categories of shrubland, crop, grassland, sparse vegetation (<15%) were regrouped to the new 'grass' category, all kinds of tree covers such as deciduous, broad-leaved, needle-leaved forests and mosaic areas were regrouped to the new 'forest' category, and the bare sandy regions were included in the new 'desert' category. After regrouping, the vegetation cover map was resampled from 300-m resolution to 5-km resolution (which is the same resolution as the GPM/DPR σ^0 maps). Because the 5-km pixel can be a mixture of old pixels with several different landcover categories, we selected the category which occupied the biggest majority inside a new pixel and assigned it as a category of the new pixel. In this process, a fraction of the new category inside each new pixel was calculated. These fraction data were to be used for extracting σ^0 data and other ancillary data for the study of σ^0 dependence on different vegetation cover types. The derived vegetation cover map is shown in Figure 1.

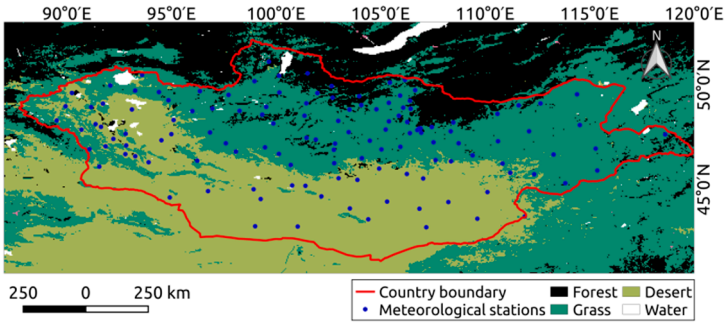


Figure 1. The vegetation map derived from the ESA-CCI 2015.

We used precipitation data for the reference of climate. They were provided by the Information and Research Institute of Meteorology, Hydrology, and Environment of Mongolia for the period of 2014–2017. Data from 129 meteorological weather stations, distributing across Mongolia (blue dots in Figure 1), were collected and grouped to the targeted vegetation covers: 27 stations in the desert, 75 stations in grassland, and 27 stations in the forest (although many of them distributed on the boundary between forest and grassland). Then we calculated monthly precipitation for each vegetation cover averaged by years 2014–2017. Another possible climate variable which can influence this study is temperature. In particular, it controls freeze/thaw of water in surface soil and vegetation. However, as we describe later, our main interest is in the summer season (May to September) in which most of the soil water and vegetation are not frozen. Therefore, we did not consider temperature as a controlling factor.

We used data of optical sensors (MODIS) for reference of the vegetation dynamics: We used LAI data from the product of "MCD15A3H Leaf Area Index/FPAR version 6 level 4, four days composite, 500 m spatial resolution" [35]. By an average resampling, we converted its resolution from 500 m to 5 km so as to set the same resolution as GPM/DPR maps. Then we calculated the time-series LAI data from January to December (four-day interval) for each vegetation category, by taking areal average in the same vegetation category and by taking an average of the four years (2014–2017) in the same four-day period. In this calculation, we only used the pixels whose fraction of its vegetation cover type was higher than 0.85. Then we compared these time-series LAI data with the seasonal σ^0 characteristics.

We also derived NDVI maps from the product of "MOD13C2 MODIS/Terra Vegetation Indices Monthly L3 Global 0.05 Deg" [36] in May–September in the years 2014 to 2018. We obtained this dataset from https://e4ftl01.cr.usgs.gov/MOLT/MOD13C2.006/ website. According to the quality assurance flag (MOD13C2 CMG 0.05 deg monthly pixel reliability), among all the NDVI data in all the monthly periods in the entire study area, 85.8% were "Good Data", 13% were "Marginal data", 0.2% were "Not Processed", 0.6% were "Snow/Ice", and no pixels were "Cloudy".

2.4. Analysis of Characteristics of GPM/DPR Signals over the Land Surface

We analyzed characteristics of σ^0 of the GPM/DPR for its dependency on the incidence angles (with 0.75° step), vegetation cover types (forest, grass, and desert), bands (Ku and Ka), and their seasonal changes. As mentioned above, we considered only the pixels of the σ^0 maps which correspond to the pixels on the reference vegetation map (derived from ESA-CCI) with a fraction higher than 0.85, because we needed to remove the influence of mixed pixels. We compared the seasonal change of σ^0 with seasonal changes of precipitation and LAI. Then, we investigated which information of GPM/DPR σ^0 was useful for the Mongolian vegetation mapping. We used the knowledge for vegetation cover mapping in the next step.

2.5. Vegetation Cover Mapping by GPM/DPR Data

By using the selected information of GPM/DPR σ^0, we performed vegetation mapping in Mongolia. First of all, we applied cubic spline spatial interpolation on each σ^0 map to fill the "no data" pixels.

As mentioned above (in Section 2.2), the σ^0 map of each incidence angle of each band in each period can contain "no data" pixels which did not have an observation in the specified conditions.

Then, we tried mapping vegetation cover of three types (forest, grass, desert) using the interpolated σ^0 map. We applied a simple unsupervised K-means clustering for σ^0 maps of KuPR and σ^0 maps of KaPR, separately, for the sake of the comparison of the capability of mapping by KuPR and KaPR. The cluster number was chosen to be $k = 4$ for each map, considering the three vegetation types and water bodies.

After that, we tried a similar mapping but in this case, using a combination of KuPR and KaPR: We merged the multi-angle interpolated σ^0 maps of KuPR and KaPR and applied principal component analysis (PCA) [37] to reduce the dimension of the feature space consisting of the multi-band, multi-angle, interpolated σ^0 maps. By PCA, we can find a small number of features, which are linear combinations of the features, keeping most of the information in the initial dataset. After performing the PCA, we tried vegetation mapping by K-means clustering on the reduced maps.

In this process, we chose an optimal cluster number by using an elbow method. The elbow method explains the sum of squared distances (SSD) of σ^0 data to their closest cluster centers. As a cluster number (k) increases, the SSD approaches to 0. The elbow method draws a plot of cluster number and SSD of σ^0 data to their closest cluster center. Then, the corner of the curve in the plot indicates the optimal value of k.

We implemented all of these analyses, including the spatial interpolation, K-means, PCA, and elbow methods, by using Python 3's Scikit-learn library (version 0.21) on Ubuntu Linux 16.04.

3. Results

3.1. Characteristics of GPM/DPR Signals over the Land Surface

Figure 2 shows characteristics of σ^0 of GPM/DPR at all incidence angles (with 0.75° step) and their seasonal changes for the three vegetation cover types (forest, grass, and desert). The seasonal variation of σ^0 at some incidence angles were compared to those of precipitation and LAI. Generally, GPM/DPR σ^0 decreased when the incidence angle increased except for the forest.

3.1.1. Forest

The angular dependency of σ^0 over the forest was plotted in Figure 2a. In summer (July, green lines), the responses of the KuPR and KaPR σ^0 were mostly the same. Both σ^0 dropped sharply from 5 dB to −7 dB at until 2°. Then, at larger angles, both σ^0 remained mostly constant at a low value around −7 dB. On the other hand, in winter (January, grey lines), a drop of KuPR σ^0 within 0° to 2° was bigger than that of KaPR σ^0, then KuPR σ^0 remained almost constant, but the KaPR σ^0 increased gradually reaching to the −1 dB at 8° incidence angle.

In the forest (Figure 2b), the seasonal variation of the precipitation reached 80 mm/month, and the variation of LAI increased from around 0 to a maximum of about 3.2 in summer, then decreased back to below 1 in winter months. At nadir, seasonal change of KuPR and KaPR σ^0 reached the highest in May to September then lower values in the rest of the months (red line in Figure 2b). At the angles of slight off-nadir (~1°, grey line in Figure 2b), little seasonal variations were observed in both KuPR and KaPR. In larger angles (at ~8°), some seasonal variations appeared in KuPR and KaPR, with an opposite pattern of the observed pattern at nadir. The seasonal variations of LAI and precipitation are similar to each other, but the period of the clear changes (June–August) was shorter than that of σ^0 (May to September).

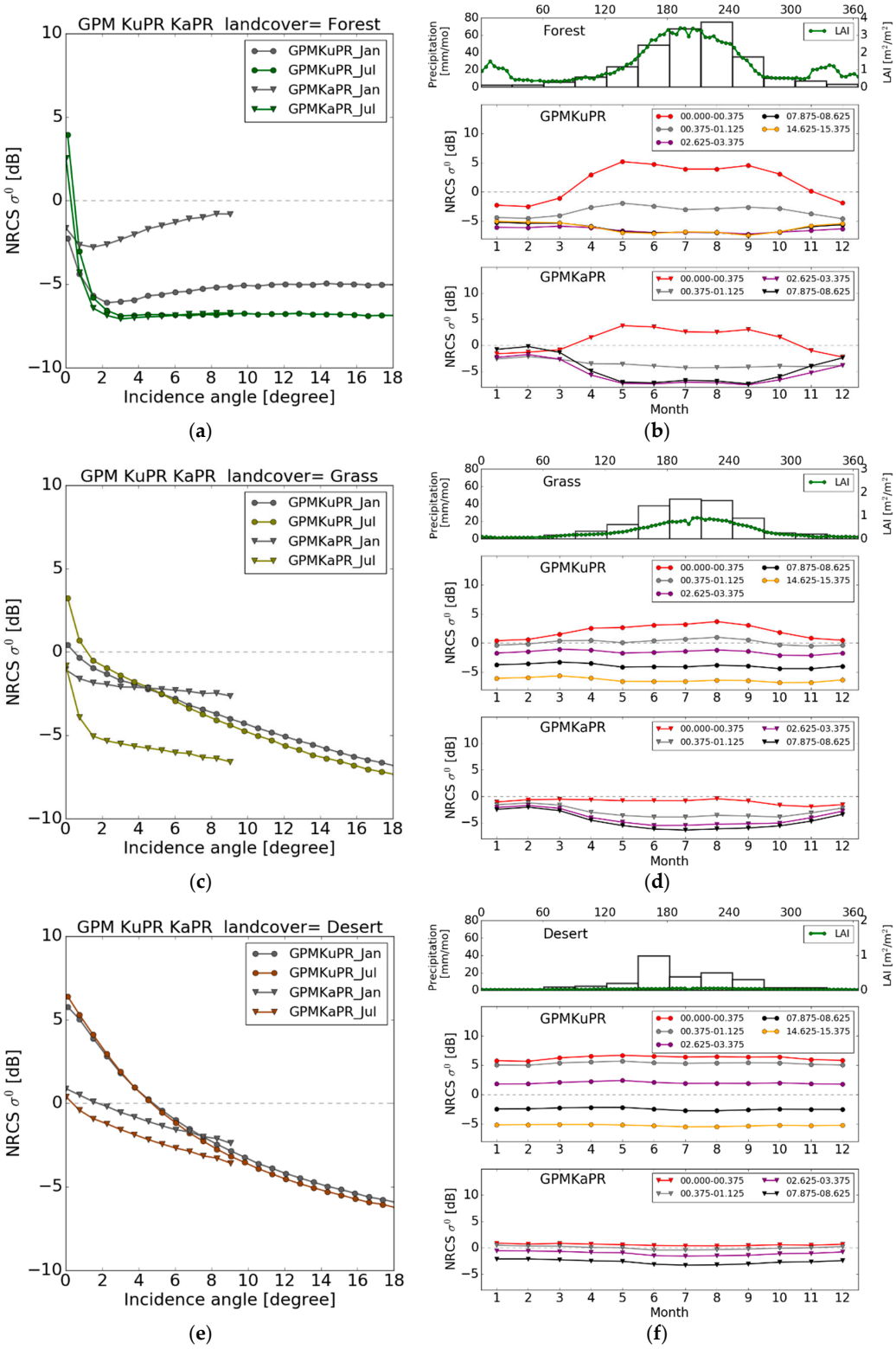


Figure 2. Characteristics of NRCS (normalized radar cross-section, described in σ^0) of KuPR and KaPR depending on angle, season, and vegetation cover, and comparison with climate and vegetation variables in 2014–2017. The incidence angle dependencies are shown in (**a**,**c**,**e**), and seasonal variations of some angles are shown in (**b**,**d**,**f**). These plots were adapted from [20].

3.1.2. Grass

Over the grass (in Figure 2c), angular dependencies of σ^0 of KuPR and KaPR are characterized by mixed characteristics of the forest and the desert (which will be shown in the next Section 3.1.3). At large angles (>2°), it was not as stable as σ^0 in the forest, whereas at small angles (<2°), it did not show the rapid decrease seen in the desert. In summer and winter, KuPR σ^0 were almost the same, but KaPR σ^0 had seasonal changes around 4 dB at higher than 2° angles.

On the other hand, the seasonal variation of LAI was below two in the summer months. The seasonal variation of KuPR σ^0 at given angles were nearly stable during all months. Particularly, their amplitude of the variations disappeared with wider angles. In contrast, KaPR σ^0 at large angles is more sensitive to seasonal change. For example, a significant seasonal change of KaPR σ^0 was observed at ~8° in the grass (black line in Figure 2d). This tendency was also seen in the case of forest (black line in Figure 2b). Therefore, it can be said that KaPR's large angle scan is more sensitive to vegetation from the seasonal aspect.

3.1.3. Desert

The angular dependency of σ^0 over the desert was plotted in Figure 2e. In the desert, σ^0 responses were mostly the same in summer and winter and decreased rapidly when the incidence angle increased. Generally, the KuPR σ^0 was relatively higher than KaPR σ^0 over the desert, but it had a more rapid decrease with larger angles. In January and July, KuPR σ^0 dropped similarly from 5 dB to −5 dB with increased angles, while drops of KaPR σ^0 had a slight gap between these two months and decreased from 0 dB to −4 dB within 0° to ~8° angles.

The desert area experiences relatively low precipitation (<40 mm/month) and much less leafy vegetation (LAI is nearly 0). In the desert, the LAI showed little seasonal variation. As expected, both KuPR and KaPR σ^0 responses over the desert were quite stable regardless of incidence angles during the year, as shown in Figure 2f. It was clear that over the desert region, the σ^0 of KuPR and KaPR at all incidence angles showed little seasonal variations.

We derived Figure 3 from Figure 2 to compare the surface characteristics of the σ^0 over the three vegetation covers by each radar. We can see that σ^0 of both KuPR and KaPR at low incidence angles, such as 1° to 8°, are useful for distinguishing vegetation density: KuPR σ^0 showed clearly lower values for the forest than others (Figure 3a), and the KaPR σ^0 showed clearly higher values for the desert than others (Figure 3b), especially at 3° and its vicinity. By combination of these two features, it may be possible to distinguish all the three vegetated covers.

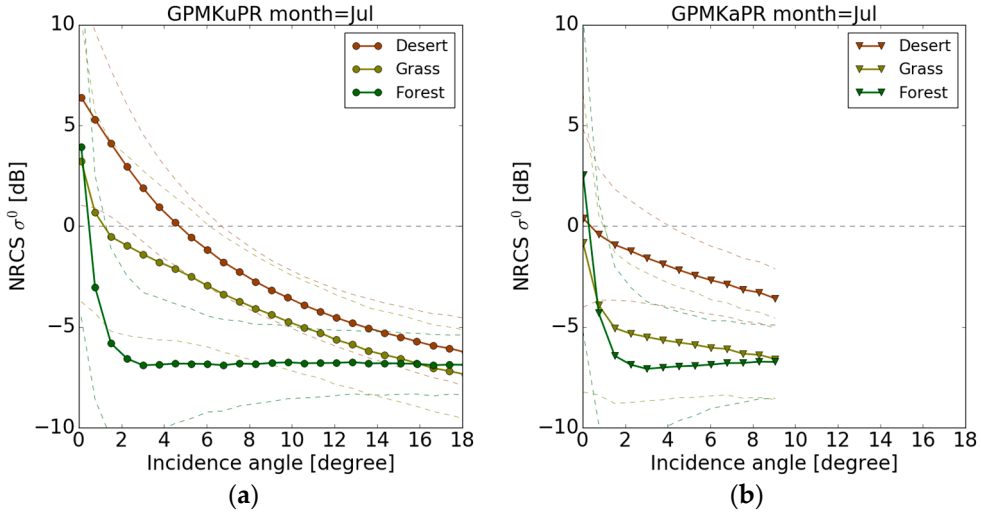


Figure 3. Comparison of angular dependency of the σ^0 over the three vegetation covers in summer (July; average of 2014–2017). Dashed lines are the standard deviation. (**a**): KuPR, (**b**): KaPR.

3.2. Vegetation Mapping by KuPR and KaPR Data Separately

Based on the findings mentioned so far, we tried vegetation mapping by a simple clustering (unsupervised classification) of GPM/DPR σ^0 at angles between 1° and 8°. In order to compare the capabilities of the two radars (KuPR and KaPR), we performed the clustering of KuPR σ^0 data and KaPR σ^0 data separately. To compare the results with the vegetation cover map (Figure 1), whose original (ESA-CCI) map was created for 2015, we performed this analysis for the year 2015. We applied the K-Means algorithm to the feature space consisting of each pixel's σ^0 values at angles between 1° and 8°. We chose the number of clusters (k) to be 4, expecting to distinguish the four dominant land cover categories: forest, grassland, desert and water bodies.

The results (both Figure 4a,b) well correspond to the vegetation cover map (Figure 1). By a closer look, we can observe the cluster #1 of KuPR (Figure 4a) corresponds well to the northern forest region in Figure 1, whereas the cluster #3 of KaPR (Figure 4b) corresponds well to the southern desert. It implies KuPR is useful for forest mapping, and KaPR is useful for desert mapping. This implication actually agrees with the findings in the previous subsection with Figure 3. By combining these advantages of KuPR and KaPR and by intersecting them, it might be possible to distinguish the grassland also.

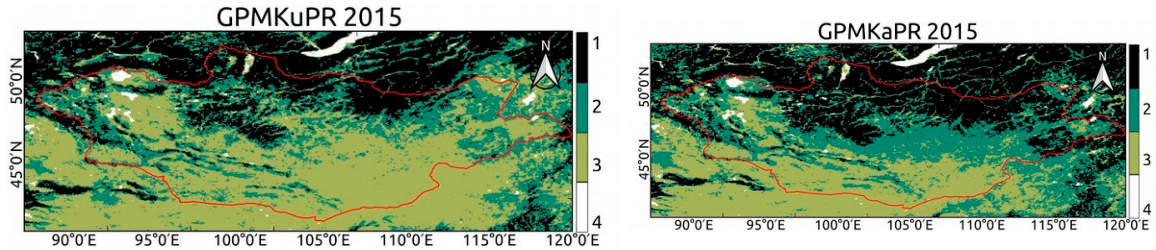


Figure 4. Cluster maps by K-means algorithm for multi-angle (1° to 8°) σ^0 of KuPR (**a**) and KaPR (**b**) with 4 clusters. GPM/DPR σ^0 data in May-September in year 2015 were used. Cluster #1 (dark green), #2 (green), #3 (yellow), and #4 (white) are supposed to be forest, grass, desert, and water, respectively.

3.3. Vegetation Mapping by Merged σ^0 Data of KuPR and KaPR

We tried a similar mapping as Section 3.2 but this time using a combination of KuPR and KaPR. First, by merging the multi-angle (between 1° and 8°, consisting of 11 angle bins), spatially-interpolated σ^0 maps of KuPR and KaPR in the summer season (May-September), we obtained a map having 22 (= 11 + 11) features. Then we applied principal component analysis (PCA) and found that PC1 (the first principle component) explained ~79%, the combination of PC1 and PC2 explained ~84%, and the combination of PC1, PC2, and PC3 explained ~88% of the total variance. From this result, we considered that the combination of PC1, PC2, and PC3 contains enough information for vegetation mapping. To validate this idea, we tried 'elbow method', which performs K-Means clustering for the various number of clusters (k) and computes the sum of squared distances (SSD) from the feature data to their closest cluster centers. As k increases, the SSD approaches to 0. This relation is plotted on a graph of k versus SSD, and the corner of the curve in the plot indicates the optimal value of k. As a result (Figure 5), the optimal cluster number was shown to be about k = 4, which corresponds to the number of our vegetation cover types. Then we performed K-Means clustering with this optimal cluster number (k = 4).

Figure 6 shows the results of the clustering. Interestingly, they (the left column) exhibit similar patterns with the yearly (average of May to September) NDVI maps (the right column). We can see the extent of the Mongolian grassland region changed significantly year by year. In particular, intensive vegetation changes occurred in the eastern part, whereas forest and the southern desert areas had little change. The central region, which is ecotone of the grassland steppe, showed some changes.

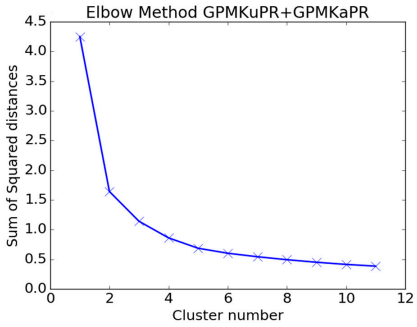


Figure 5. Elbow method plot for optimal cluster number k. Sum of squared distances unit: dB^2.

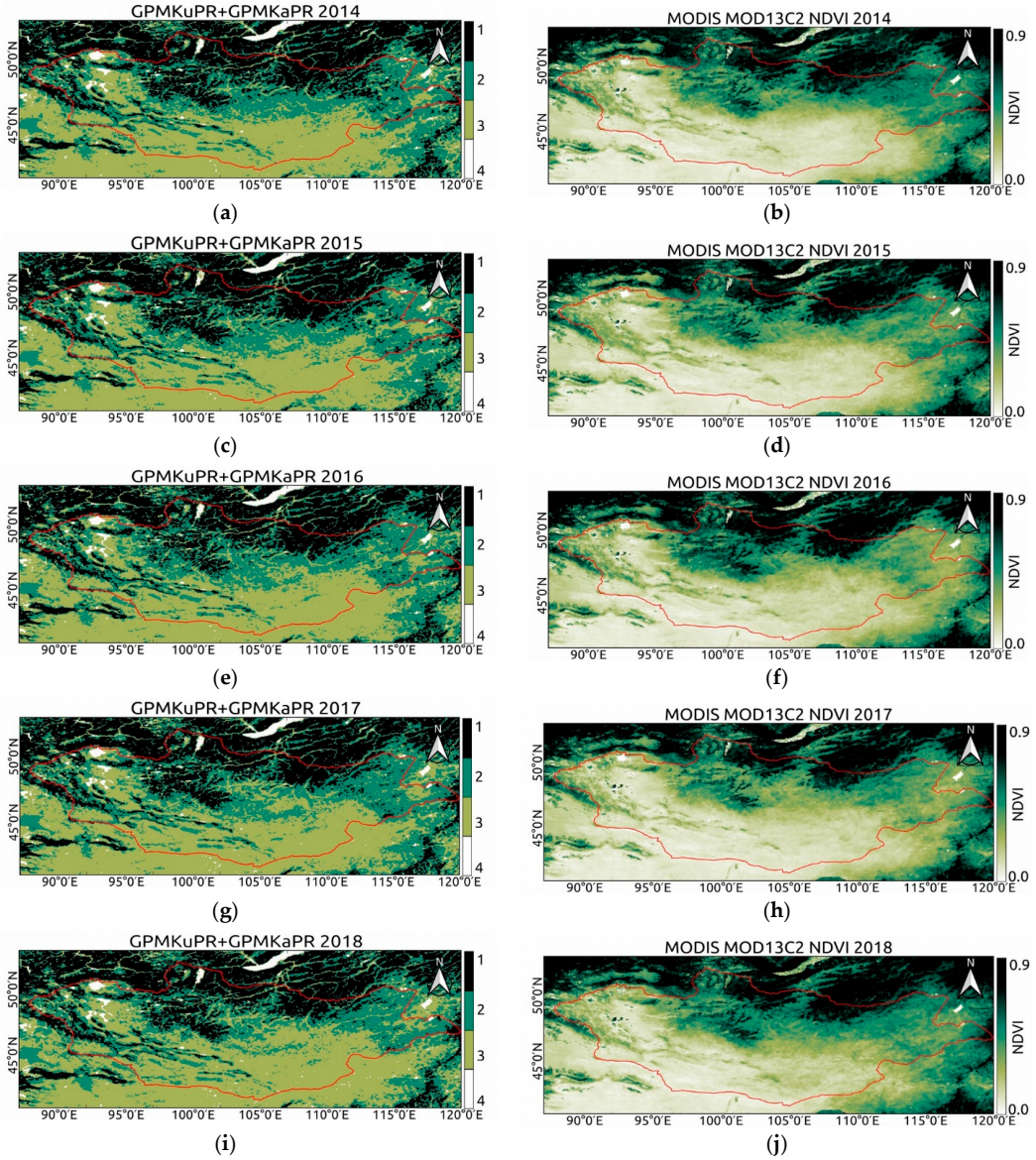


Figure 6. (**a**,**c**,**e**,**g**,**i**): Cluster maps for four clusters using a combination of PC1, PC2, and PC3 of GPM/DPR data, consisting of KuPR σ^0 at 1°–8°, KaPR σ^0 at 1°–8°, composite in May-September in years 2014-2018. For comparison, (**b**,**d**,**f**,**h**,**j**) show NDVI maps derived in the same period. Colors are chosen so that they resemble each other and Figure 1, for the convenience of comparison. In comparison to Figure 1, cluster #1 is prevailing in the forest, cluster #2 is prevailing in grassland, and cluster #3 corresponds to the desert.

Figure 7 shows the changes in GPM/DPR cluster and MODIS NDVI with respect to year 2014. For GPM/DPR clusters, because the cluster ID# increases (1 to 3) with decreasing vegetation (from forest to desert), a positive value means a decrease in vegetation, whereas a negative value means an increase in vegetation. On the other hand, for NDVI, because it is positively correlated with vegetation amount, a positive value in the difference maps means an increase in vegetation, whereas a negative value means a decrease in vegetation.

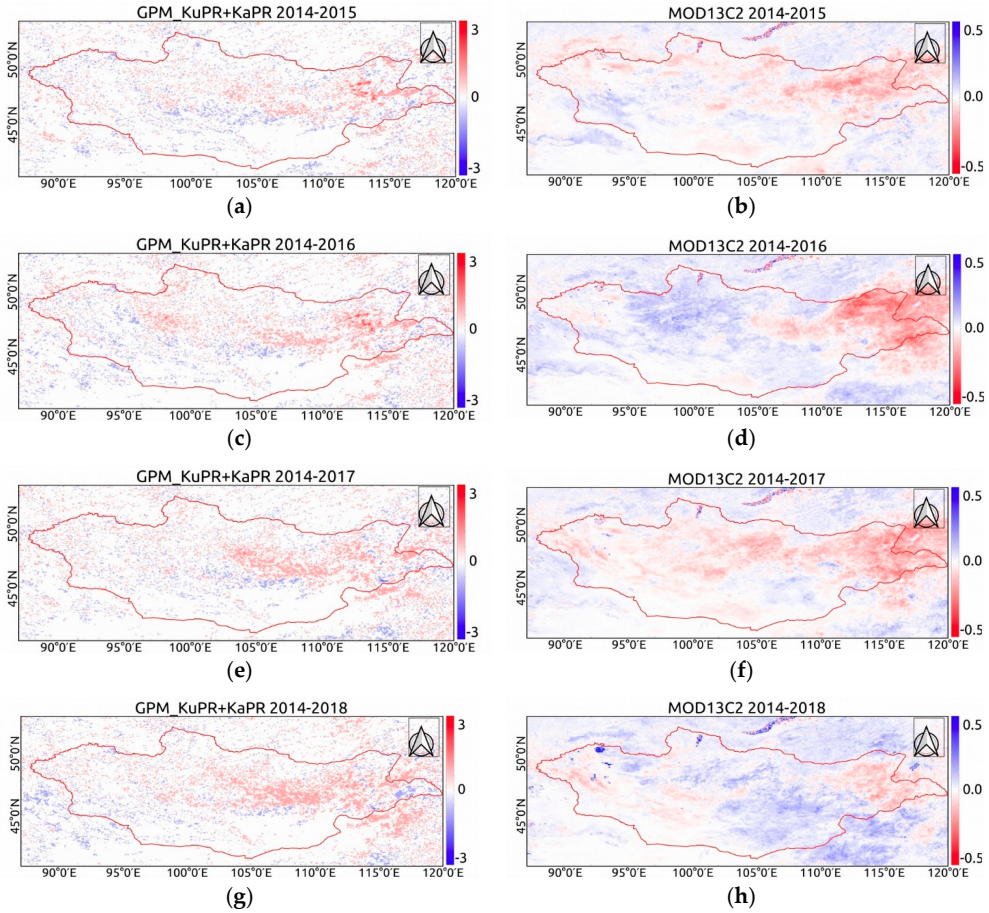


Figure 7. Change maps of GPM/DPR cluster and MODIS NDVI with respect to the year 2014. (**a**,**c**,**e**,**g**): Subtraction of the cluster ID# of 2014 from the cluster ID# of 2015, 2016, 2017, and 2018, respectively. Because the cluster ID# increases (1 to 3) with decreasing vegetation (from forest to desert), a positive value means a decrease in vegetation, whereas a negative value means an increase in vegetation. (**b**,**d**,**f**,**h**): Subtraction of NDVI values of 2014 from NDVI values of 2015, 2016, 2017, 2018. A positive value means an increase in vegetation, whereas a negative value means a decrease in vegetation.

4. Discussion

In the discussion section firstly, we highlight the main points of GPM/DPR σ^0 characteristics from the land surface, considering their agreements with the other studies, including ground radar experiments of Ku and Ka bands. In the second part, we demonstrate the significance of the DPR vegetation mapping results with its pros and cons in comparison to the NDVI maps. Finally, we point out some limitations and improvement ideas for the proposed approach.

4.1. GPM/DPR Backscatter Characteristics

The land surface σ^0 acquired by KuPR and KaPR of the GPM/DPR showed significant characteristics over the different vegetation covers in Mongolia. The Ku and Ka bands have been mostly used for the ocean and atmospheric studies and seldom used for land observation. Through analyzing the relation

of GPM/DPR $\sigma^{0'''}$'s responses with incidence angle and seasonal variation, some conclusions can be drawn as follows:

For both KuPR and KaPR σ^0, the amplitude of seasonal changes was the largest around the 8° incidence angle. It indicates that this angle is useful for detecting seasonal changes of the land surface. Although the use of a large off-nadir angle may result in a larger footprint (cell size on the ground), the actual consequence of this effect is, for the case of incidence angle of 8°, making the footprint about only 2% larger than nadir. We consider it as a negligible effect.

On the other hand, σ^0 was fairly stable and constant during the period from May to September, which is the peak growing season of vegetation in Mongolia. Therefore, we may be able to utilize σ^0 in this period for vegetation mapping in Mongolia.

It was notable that the σ^0 values at forest were relatively low and constant over a wide range of incidence angles except for the nadir. However, at the desert, σ^0 values were relatively higher and kept decreasing with the increase of the incidence angles. These features are corroborated by the previous studies, including the Ku-band radar of TRMM/PR [18] and Ulaby et al. [38].

In Ulaby et al. (2014, Figure 11-15, [38]), Ku-band (13 GHz) backscatter ground radar experiments were conducted over short and tall alfalfa canopies, which are somehow similar to Mongolian grass and forest steppe. As expected, similarities are observed between the Ku-band ground radar and satellite radar (KuPR) at angles below 20°. For example, the ground radar backscatter from the sparse vegetation was relatively higher, but decreased rapidly with wider incidence angle, while the backscatter of dense vegetation remained stable. Similar characteristics can be seen for KuPR σ^0 in Figure 3a. More similarity is that in Figure 3a, the KuPR σ^0 plots of the three vegetation covers intersected at around 18° and equivalently the ground radar measurements from two different canopies also intersected at 20° incidence angle. In addition, ground radar backscatter over the Kansas deciduous trees (Ulaby et al., 2014, Figure 11-51, [38]) was constant at around −8 dB. This agrees with the KuPR σ^0 over the forest in our study (Figure 3). In summary, our results of the KuPR σ^0 are consistent with the experiments of Ku-band ground radar.

According to the ground experiment of Ka-band radar (Ulaby et al., 2014, Figure 10-20 and Figure 10-21, [38]), σ^0 values at dry asphalt were within 10 to 0 dB, whereas σ^0 values at loose dirt bare surface were within 0 to −10 dB at the incidence angle lower than 10°. Our GPM/KaPR σ^0 values over the desert were in between these two experiments. It is reasonable because the desert cover is softer than asphalt and harder than the loose dirt surface.

Moreover, many studies revealed that microwave backscatter is related to soil moisture. Prigent et al. [11] mentioned backscatter at low incidence angles (<20°) was related to soil characteristics and these angles exhibited a larger scatter. In Mongolia, a balance between the precipitation and evapotranspiration determines the soil moisture which is relatively low. Nandintsetseg et al. [27] studied seasonal variation of soil moisture for 20 years from three main vegetation zones. Following the gradient of the precipitation distribution, soil moisture decreased from the northern part to the southern part in Mongolia. However, in their study, patterns of seasonal variation of soil moisture and precipitation were different: In winter months, the soil was frozen (so that it cannot be measured). The soil moisture increased from March to April due to snowmelt, then decreased until May because the warm temperature led to the high evapotranspiration. From May to August, soil moisture increased along with precipitation. However, GPM/KuPR and KaPR σ^0 observations did not show such a clear behavior from May to August (Figure 2b,d,f). It implies that the influence of soil moisture on our GPM/DPR σ^0 data may not be evident, mainly due to eliminating the wet pixels by using the precipitation flags. However, more studies on the influence of soil moisture and canopy surface moisture (such as dew) are necessary.

4.2. Vegetation Mapping

Based on detected vegetation characteristics, vegetation maps were created by using GPM/DPR. Interestingly, general similarities were observed between our GPM/DPR based annual vegetation maps

and the NDVI maps (Figure 6): The northern forest, middle grassland, southern desert, and water bodies were sufficiently discriminated in the GPM/DPR vegetation maps. The inter-annual vegetation dynamics were also described by the GPM/DPR based maps as the NDVI maps.

An advantage of the GPM/DPR is considered to be the sensitivity to the dense canopy without saturation. In fact, in the GPM/DPR vegetation maps, the river banks and valleys inside the forest region clearly appeared over the northern forest, but not in the NDVI maps. The distribution pattern and dynamics of the grassland almost coincided with the NDVI maps in all years. Significant degradation of the grassland and expansion of the desert was observed in the central region in 2018 in both NDVI and GPM/DPR vegetation maps. The intense vegetation dynamics had been observed around the Dornod province which is located in the most eastern part of Mongolia since 2015.

In Figure 7, wide area (the central to eastern part, mostly the grasslands in Figure 1) of a decrease in vegetation can be seen both in GPM/DPR and NDVI for all the years. However, their positions are somehow different: The areas are located more in the north in NDVI and more in the south in GPM/DPR. It indicates a different sensitivity to vegetation dynamics of GPM/DPR and NDVI.

We chose three sites from the study area for more investigation of yearly changes of σ^0 (Figure 8). The first site (site A) contains the saxaul forest which may not be determined by NDVI but may be detected by the GPM/DPR. The second site (site B) is the central part of Mongolia containing grasslands with a large inter-annual change. The third site (site C) is in the main grass and desert where extensive dynamics have been observed.

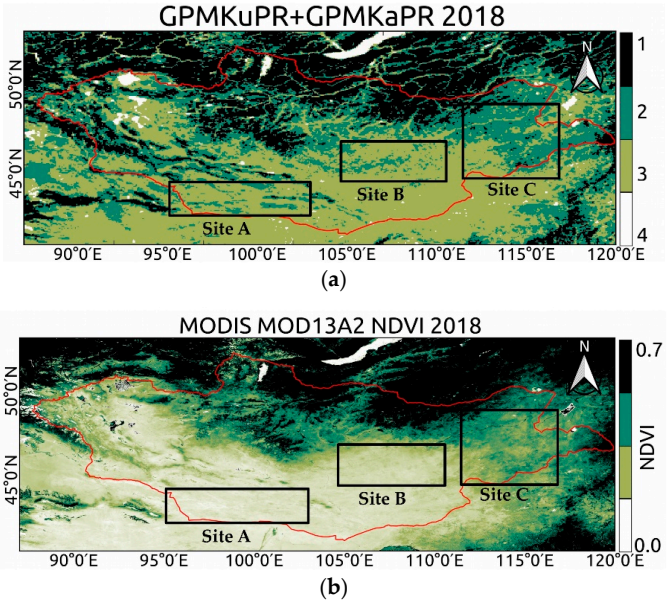


Figure 8. Three sites for more investigation of yearly changes of σ^0. The backdrops of (**a**,**b**) are Figure 6i,j, respectively.

Because NDVI can only indicate the productive vegetation [39], less productive desert plants cannot be distinguished well by NDVI. The GPM/DPR may be able to detect it more effectively from a structural aspect. One possible example is the monitoring of the saxaul forest distributed in a southwestern desert area (Site A in Figure 8). This sparse forest is composed of less productive brushwood plants but it is important for a desert ecosystem (Figure 9). However, there have been few studies for the saxaul forests over Mongolia using satellite remote sensing, probably because of little sensitivity of the optical vegetation indices to the saxaul forests. In fact, the NDVI maps did not describe the saxaul forests in the south-west region, while the GPM/DPR vegetation maps showed some signals related to vegetation in this region, although some of them might be fake signals caused by mountainous topography.



Figure 9. Field photos of a saxaul forest in the Gobi Desert.

In Figure 10, the summer average σ^0 (at 3° and 8° for both KuPR and KaPR), NDVI, and precipitation were plotted for the three sites (outlined in Figure 8). In Site A and Site B, σ^0 at 3° (solid blue and black lines) followed a similar pattern to NDVI (solid green line), and σ^0 at 8° (dashed lines) was mostly constant. However, the eastern grassland (Site C) showed a drop in NDVI in 2016 (Figure 10c). This phenomenon may not be related to the condition of the grasslands. Because precipitation in 2016 did not drop, and the condition of the grasslands is strongly related to precipitation, it may be errors due to atmospheric aerosols. On the other hand, σ^0 in 2016 in this site did not show apparent changes from other years. This can be an example in which σ^0 compensates the weakness of NDVI.

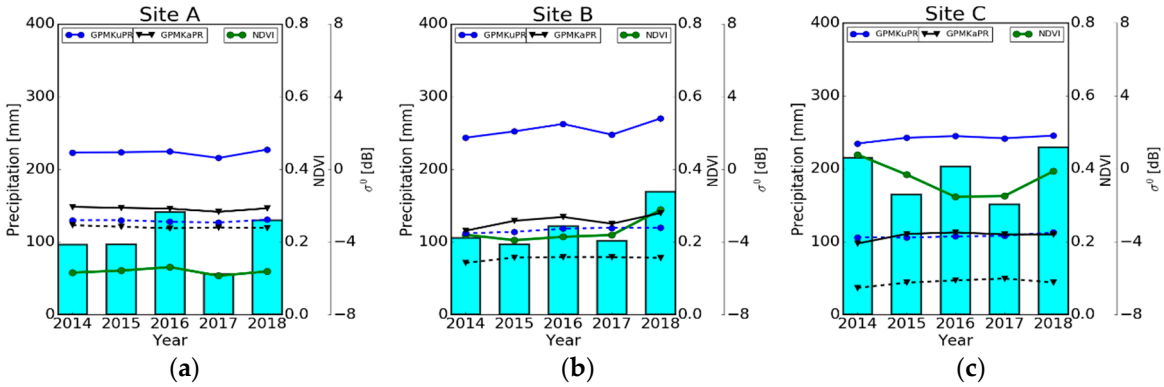


Figure 10. (**a**–**c**): Average KuPR and KaPR σ^0 at 3° (solid line) and 8° (dashed line), average MODIS NDVI (solid green line), and precipitation for each summer season (May–September) of years from 2014 to 2018 for the three sites outlined in Figure 8. NDVI and σ^0 share the right-hand vertical axis.

The main disadvantage in this study is little consideration of the topography effect to the radar backscatter. By assuming the Mongolian grassland covers fairly flat and homogeneous with respect to the DPR's small incidence angle, we directly classified the σ^0 values without any slope correction. However, there are some mountainous regions in Mongolia, and that rugged mountainous topography with little vegetation might have been classified as forests, due to strong radar backscatter on the tilted slopes. In fact, gamma0 (γ°) [40] which is commonly used in SAR study for vegetation, incorporating the incidence angle to the slope, maybe a better representation of the radar backscatter for vegetation.

Another problem is the coarse temporal resolution of single angle observations. Interpolation of data in terms of temporal, spatial, and angular directions needs further development.

5. Conclusions

This is the primary study to observe vegetation by the space-borne precipitation radar, DPR, onboard the GPM core satellite over Mongolian land, which is a novel method to broaden the existing common optical and microwave approaches. We characterized the backscatter (σ^0) of GPM/DPR's two microwave bands (Ku and Ka) with respect to the dominant vegetation zones (forest, grassland, desert) over Mongolia. The dependence of radar backscatter on the incidence angles offers plenty

of information about vegetation dynamics. Both Ku and Ka radar's σ^0 values were investigated for incidence angle dependency and the seasonal variation. As a result, the use of multi-angle, multi-band observations of GPM/DPR can help to characterize the vegetation zones. Especially, the σ^0 at incidence angles between 1° and 8° represented sufficient characteristics of vegetation. They showed the significant discrimination of vegetation zones and sufficiently detected the inter-annual dynamics. In other words, they indicated that Mongolia experienced extensive changes in grassland and desert areas during the study years. Thus, it revealed the utility of the GPM/DPR not only for precipitation but also for land surface study.

Although the physical mechanism of optical sensors and precipitation radars are totally different, the vegetation maps derived from the data of a precipitation radar (GPM/DPR) are closely consistent with NDVI maps derived from data of an optical sensor (MODIS). It means precipitation radars can work as a "back-up" of optical sensors by giving evidence of vegetation dynamics separated from the noise and bias introduced by atmospheric particles. Moreover, the spatial patterns of changes detected in GPM/DPR data and NDVI data were somehow different from each other, indicating the unique utility of GPM/DPR data for vegetation dynamics study. Further study is desired for investigation of the utility of the precipitation radars (GPM/DPR as well as TRMM/PR) in various climate zones including more humid and temperate areas.

Author Contributions: B.N. performed the data analysis and wrote the main parts of the manuscripts. K.N.N. created the general concept and design for this study. T.K. and T.M. contributed to the engineering part of the use of GPM/DPR data. The data collection and discussion about Mongolian geography was contributed by B.N.

Funding: We thank the Project for Human Resource Development Scholarship (JDS) by Japanese Grant Aid (No. B0012017MNG006). This research is supported by the Ecosystem Group of Earth Observation Research Center (EORC) of JAXA.

Acknowledgments: The corresponding authors appreciate Information and Research Institute Meteorology Hydrology and Environment (IRIMHE) for providing meteorological station's precipitation data and thank MSc. Narangerel (IRIMHE) for sharing field photos of saxaul forest in the Gobi Desert. We wish to acknowledge the anonymous reviewers that helped improve this paper with their comments and suggestions.

Conflicts of Interest: The authors declare no conflict of interest.

References

1. Xie, Y.; Sha, Z.; Yu, M. Remote sensing imagery in vegetation mapping: A review. *J. Plant Ecol.* **2008**, *1*, 9–23. [CrossRef]
2. Zhou, X.; Yamaguchi, Y. Relative importance of climatic and anthropogenic drivers on the dynamics of aboveground biomass across agro-ecological zones on the Mongolian Plateau. *Sustainability* **2018**, *10*, 3435. [CrossRef]
3. Liu, Y.Y.; Evans, J.P.; McCabe, M.F.; de Jeu, R.A.M.; van Dijk, A.I.J.M.; Dolman, A.J.; Saizen, I. Changing Climate and Overgrazing Are Decimating Mongolian Steppes. *PLoS ONE* **2013**, *8*, e57599. [CrossRef] [PubMed]
4. Liu, Y.Y.; De Jeu, R.A.M.; McCabe, M.F.; Evans, J.P.; Van Dijk, A.I.J.M. Global long-term passive microwave satellite-based retrievals of vegetation optical depth. *Geophys. Res. Lett.* **2011**, *38*, 1–6. [CrossRef]
5. Hilker, T.; Natsagdorj, E.; Waring, R.H.; Lyapustin, A.; Wang, Y. Satellite observed widespread decline in Mongolian grasslands largely due to overgrazing. *Glob. Chang. Biol.* **2014**, *20*, 418–428. [CrossRef]
6. Li, C.; Filho, W.L.; Wang, J.; Yin, J.; Fedoruk, M.; Bao, G.; Bao, Y.; Yin, S.; Yu, S.; Hu, R. An assessment of the impacts of climate extremes on the vegetation in Mongolian Plateau: Using a scenarios-based analysis to support regional adaptation and mitigation options. *Ecol. Indic.* **2018**, *95*, 805–814. [CrossRef]
7. Tucker, C.J.; Sellers, P.J. Satellite remote sensing of primary production. *Int. J. Remote Sens.* **1986**, *7*, 1395–1416. [CrossRef]
8. Myneni, R.B.; Hall, F.G.; Sellers, P.J.; Marshak, A.L. Interpretation of spectral vegetation indexes. *IEEE Trans. Geosci. Remote Sens.* **1995**, *33*, 481–486. [CrossRef]

9. Liu, Y.Y.; van Dijk, A.I.J.M.; McCabe, M.F.; Evans, J.P.; de Jeu, R.A.M. Global vegetation biomass change (1988-2008) and attribution to environmental and human drivers. *Glob. Ecol. Biogeogr.* **2013**, *22*, 692–705. [CrossRef]
10. Kasischke, E.S.; Melack, J.M.; Dobson, M.C. The use of imaging radars for ecological applications—A review. *Remote Sens. Environ.* **1997**, *52*, 141–156. [CrossRef]
11. Prigent, C.; Aires, F.; Rossow, W.; Matthews, E. Joint characterization of vegetation by satellite observations from visible to microwave wavelengths: A sensitivity analysis. *J. Geophys. Res. Atmos.* **2001**, *106*, 20665–20685. [CrossRef]
12. Du, J.; Kimball, J.S.; Jones, L.A.; Kim, Y.; Glassy, J.; Watts, J.D. A global satellite environmental data record derived from AMSR-E and AMSR2 microwave Earth observations. *Earth Syst. Sci. Data* **2017**, *9*, 791. [CrossRef]
13. Benninga, H.-J.F.; van der Velde, R.; Su, Z. Impacts of Radiometric Uncertainty and Weather-Related Surface Conditions on Soil Moisture Retrievals with Sentinel-1. *Remote Sens.* **2019**, *11*, 2025. [CrossRef]
14. Amazirh, A.; Merlin, O.; Er-Raki, S.; Gao, Q.; Rivalland, V.; Malbeteau, Y.; Khabba, S.; Escorihuela, M.J. Retrieving surface soil moisture at high spatio-temporal resolution from a synergy between Sentinel-1 radar and Landsat thermal data: A study case over bare soil. *Remote Sens. Environ.* **2018**, *211*, 321–337. [CrossRef]
15. Lillesand, T.M.; Kiefer, R.W. *Remote Sensing and Image Interpretation*, 7th ed.; John Wiley & Sons: Hoboken, NJ, USA, 2015.
16. Hou, A.Y.; Kakar, R.K.; Neeck, S.; Azarbarzin, A.A.; Kummerow, C.D.; Kojima, M.; Oki, R.; Nakamura, K.; Iguchi, T. The global precipitation measurement mission. *Bull. Am. Meteorol. Soc.* **2014**, *95*, 701–722. [CrossRef]
17. Kubota, T.; Yoshida, N.; Urita, S.; Iguchi, T.; Seto, S.; Meneghini, R.; Awaka, J.; Hanado, H.; Kida, S.; Oki, R. Evaluation of precipitation estimates by at-launch codes of GPM/DPR algorithms using synthetic data from TRMM/PR Observations. *IEEE J. Sel. Top. Appl. Earth Obs. Remote Sens.* **2014**, *7*, 3931–3944. [CrossRef]
18. Kummerow, C.; Barnes, W.; Kozu, T.; Shiue, J.; Simpson, J. The Tropical Rainfall Measuring Mission (TRMM) sensor package. *J. Atmos. Ocean. Technol.* **1998**, *15*, 809–817. [CrossRef]
19. Kozu, T.; Kawanishi, T.; Kuroiwa, H.; Kojima, M.; Oikawa, K.; Kumagai, H.; Okamoto, K.N.I.; Okumura, M.; Nakatsuka, H.; Nishikawa, K. Development of precipitation radar onboard the Tropical Rainfall Measuring Mission (TRMM) satellite. *IEEE Trans. Geosci. Remote Sens.* **2001**, *39*, 102–116. [CrossRef]
20. Nagaoka, J.; Yamamoto, M.K.; Higuchi, A.; Sensing, E.R. *Characteristics of Backscattering Coefficients over Different Vegetation Land Covers Derived from TRMM/PR*; Chiba University: Chiba, Japan, 2009; pp. 146–149.
21. Prigent, C.; Aires, F.; Jimenez, C.; Papa, F.; Roger, J. Multiangle backscattering observations of continental surfaces in Ku-band (13 GHz) from satellites: Understanding the signals, particularly in arid regions. *IEEE Trans. Geosci. Remote Sens.* **2015**, *53*, 1364–1373. [CrossRef]
22. Leland, C.; Lyon, B.; Wang, S.-Y.; Davi, N.K.; D'Arrigo, R.D.; Rao, M.P.; Byambasuren, O.; Nachin, B.; Skees, J. Dzuds, droughts, and livestock mortality in Mongolia. *Environ. Res. Lett.* **2015**, *10*, 074012.
23. Zhou, X.; Yamaguchi, Y.; Arjasakusuma, S. Distinguishing the vegetation dynamics induced by anthropogenic factors using vegetation optical depth and AVHRR NDVI: A cross-border study on the Mongolian Plateau. *Sci. Total Environ.* **2018**, *616–617*, 730–743. [CrossRef] [PubMed]
24. Batima, P.; Natsagdorj, L.; Gombluudev, P.; Erdenetsetseg, B. Observed climate change in Mongolia. Assessments and Adaptations to Climate Change (AIACC). *AIACC Work. Pap.* **2005**, *12*, 1–26.
25. Nanzad, L.; Zhang, J.; Tuvdendorj, B.; Nabil, M.; Zhang, S.; Bai, Y. NDVI anomaly for drought monitoring and its correlation with climate factors over Mongolia from 2000 to 2016. *J. Arid Environ.* **2019**, *164*, 69–77. [CrossRef]
26. Klinge, M.; Dulamsuren, C.; Erasmi, S.; Karger, D.N.; Hauck, M. Climate effects on the vitality of boreal forests at the treeline in different ecozones of Mongolia. *Biogeosci. Discuss.* **2017**, 1–25. [CrossRef]
27. Nandintsetseg, B.; Shinoda, M. Seasonal change of soil moisture in Mongolia: Its climatology and modelling. *Int. J. Climatol.* **2011**, *31*, 1143–1152. [CrossRef]
28. Dorjsuren, M.; Liou, Y.-A.; Cheng, C.-H. Time Series MODIS and in Situ Data Analysis for Mongolia Drought. *Remote Sens.* **2016**, *8*, 509. [CrossRef]
29. John, R.; Chen, J.; Giannico, V.; Park, H.; Xiao, J.; Shirkey, G.; Ouyang, Z.; Shao, C.; Lafortezza, R.; Qi, J. Grassland canopy cover and aboveground biomass in Mongolia and Inner Mongolia: Spatiotemporal estimates and controlling factors. *Remote Sens. Environ.* **2018**, *213*, 34–48. [CrossRef]

30. Suvdantsetseg, B. Saxaul Forest Area Determination by Remote Sensing in Mongolia's Gobi Region. *Int. Arch. Photogramm. Remote Sens. Spat. Inf. Sci.* **2008**, *XXXVII Pt B8*.
31. Nasanbat, E.; Lkhamjav, O.; Balkhai, A.; Tsevee-Oirov, C.; Purev, A.; Dorjsuren, M. A spatial distributionmap of the wildfire risk in Mongolia using decision support system. *Int. Arch. Photogramm. Remote Sens. Spatial Inf. Sci.* **2018**, *XLII-3/W4*, 357–362. [CrossRef]
32. Sato, T.; Kimura, F.; Kitoh, A. Projection of global warming onto regional precipitation over Mongolia using a regional climate model. *J. Hydrol.* **2007**, *333*, 144–154. [CrossRef]
33. Iguchi, A.T.; Seto, S.; Meneghini, R.; Yoshida, N.; Awaka, J.; Le, M.; Chandrasekar, V.; Brodzik, S.; Kubota, T. *GPM/DPR Level-2 Algorithm Theoretical Basis Document*; NASA Goddard Space Flight Center: Greenbelt, MD, USA, 2018.
34. Poulter, B.; MacBean, N.; Hartley, A.; Khlystova, I.; Arino, O.; Betts, R.; Hagemann, S. Plant functional type classification for earth system models: results from the European Space Agency's Land Cover Climate Change Initiative. *Geosci. Model Dev.* **2015**, *8*, 2315–2328. [CrossRef]
35. Myneni, R.; Knyazikhin, Y.; Park, T. MCD15A3H MODIS/Terra+Aqua Leaf Area Index/FPAR 4-day L4 Global 500m SIN Grid V006. *NASA EOSDIS Land Process. DAAC* **2015**. [CrossRef]
36. Didan, K. MOD13C2 MODIS/Terra Vegetation Indices Monthly L3 Global 0.05Deg CMG V006. *NASA EOSDIS Land Process. DAAC* **2015**. [CrossRef]
37. Durden, S.L.; Tanelli, S.; Meneghini, R. Using surface classification to improve surface reference technique performance over land. *Indian J. Radio Space Phys.* **2012**, *41*, 403–410.
38. Ulaby, F.; Long, D. *Microwave Radar and Radiometric Remote Sensing*; University of Michigan Press: Ann Arbor, MI, USA, 2014.
39. Andela, N.; Liu, Y.Y.; Van Dijk, A.I.J.M.; De Jeu, R.A.M.; McVicar, T.R. Global changes in dryland vegetation dynamics (1988-2008) assessed by satellite remote sensing: Comparing a new passive microwave vegetation density record with reflective greenness data. *Biogeosciences* **2013**, *10*, 6657–6676. [CrossRef]
40. Small, D. Flattening gamma: Radiometric terrain correction for SAR imagery. *IEEE Trans. Geosci. Remote Sens.* **2011**, *49*, 3081–3093. [CrossRef]



© 2019 by the authors. Licensee MDPI, Basel, Switzerland. This article is an open access article distributed under the terms and conditions of the Creative Commons Attribution (CC BY) license (http://creativecommons.org/licenses/by/4.0/).